

Vacancy tuned thermoelectric properties and high spin filtering performance in graphene/silicene heterostructures

Zainab Gholami and Farhad Khoeini*

Department of physics, University of Zanjan, P.O. Box 45195-313, Zanjan, Iran

Abstract

The main contribution of this paper is to study the spin caloritronic effects in defected graphene/silicene nanoribbon (GSNR) junctions. Each step-like GSNR is subjected to the ferromagnetic exchange and local external electric fields, and their responses are determined using the nonequilibrium Green's function (NEGF) approach. To further study the thermoelectric (TE) properties of the GSNRs, three defect arrangements of divacancies (DVs) are also considered for a larger system, and their responses are re-evaluated. The results demonstrate that the defected GSNRs with the DVs can provide an almost perfect thermal spin filtering effect (SFE), and spin switching. A negative differential thermoelectric resistance (NDTR) effect and high spin polarization efficiency (SPE) larger than 99.99% are obtained. The system with the DV defects can show a large spin-dependent Seebeck coefficient, equal to $S_s \sim 1.2$ mV/K, which is relatively large and acceptable. Appropriate thermal and electronic properties of the GSNRs can also be obtained by tuning up the DV orientation in the device region. Accordingly, the step-like GSNRs can be employed to produce high efficiency spin caloritronic devices with various features in practical applications.

Keywords: Spin caloritronics, Thermal spin-filtering, Parallel step-like junction, Divacancy defect, Nonequilibrium Green's function.

1. Introduction

The next generation of electronic devices is often required to possess high performance, minimum waste heat, and low dimension in practical applications¹⁻⁴. The spin caloritronics, as a new branch of spintronics, focuses on the relationship between the heat and spin transports in the material and attempts to pave the way for the development of nanostructure devices in the heat sensors, waste heat recyclers, and future device technologies⁵⁻⁷. The spin-dependent

Seebeck effect (SDSE), as an essential feature of the spin caloritronics, aims to produce spin-polarized currents by using the temperature gradient. This can efficiently help us to obtain a pure spin current with no charge companions. The spin equivalent of the classical Seebeck effect was first observed by Uchida *et al.*⁸ in the ferromagnetic metals. Numerous studies were then performed by other researchers on quasi-one or two-dimensional (2D) materials such as graphene (GE), silicene (SE), MoS₂, and so on⁹⁻¹². Although nanoribbon materials with zigzag edges have inherent antiferromagnetic properties, they can be magnetized by using an external magnetic field. This can provide us to understand well SDSE and thermal spin transport attributes of such types of materials (e.g., spin-dependent Seebeck diode (SSD) effect, thermal SFE, and thermal spin-giant-magnetoresistance (GMR) effect¹³⁻¹⁵).

GE and SE are now introduced as the famous family of low-dimensional materials¹⁶⁻¹⁸ with unusual features for the next generation of device applications^{19,20}. They consist of a honeycomb structure with promising electronic properties such as high carrier mobility²¹⁻²⁴. GE and SE nanostructures are now identified as materials with adequate Seebeck coefficient and widespread spin caloritronics applications^{21,23-25}. Quasi-one-dimensional structures, theoretically, show satisfactory thermoelectric performance compared to 2D structures²⁶. This may be attributed to the fact that cutting a 2D material into a nanoribbon can decrease the thermal conductivity and lead to better thermoelectric properties. A GE-based thermoelectric device was experimentally introduced by Sierra *et al.*²⁷, to produce a spin voltage via two ferromagnetic thermal sources with variant temperatures. However, GE is not often identified as an efficient thermoelectric material, because it shows a low figure of merit (FOM)²⁸. In contrast, SE has superior thermoelectric properties than GE and can drastically enhance the Seebeck coefficient, due to its nonzero band gap^{24,29}. According to previous studies, the zigzag SE nanoribbons (ZSNRs) can suitably provide a significant spin filter efficiency³⁰, and a perfect SDSE⁹. The thermoelectric performance of nanostructures can also be enhanced by various ways, such as hybridization^{31,32}, defects³³⁻³⁵, and doping^{36,37}. As shown in the previous studies^{4,38,39}, the hybrid nanostructures theoretically show superior thermoelectric properties than the similar materials with the single nanostructures. Several studies have already been performed to investigate various properties of the GSNRs in which GE and SE have vertically or laterally bonded together⁴⁰⁻⁴³. The results showed that the combination of GE with other 2D materials could lead to a hybrid structure with various properties and applications⁴⁴⁻⁴⁷. Nevertheless, there are little data about the electronic behavior, spin transport, and thermoelectric attributes of the GSNRs^{38,46}, and further research is still required in this area.

Several studies have been conducted to investigate the effect of structural defects and pattern geometry on the thermal and thermoelectric phenomena of nanoribbons^{10,48-50}. Experimental results clearly show that the thermal conductivity of GE with a patterned vacancy (nanomesh) structure is significantly lower than that observed by the pristine GE⁵¹. In addition, nanoribbons with periodic edge defects, called saw tooth-like (ST)⁵², can also improve the spin thermoelectric properties, identified by the large values of spin-dependent Seebeck coefficient and FOM⁵³. Some designs have been used to connect the GE flake to two armchair GE nanoribbons (AGNRs), and to generate spin-dependent currents^{54,55}. The width of the nanoribbon, the coupling between the leads and the ribbon, and the topology were also identified as the main factors affecting the electrical and thermal properties of the nanoribbon. Sonvane *et al.* showed that the thermal transport of a GNR could significantly be affected by changing its length or width⁵⁶. Some unusual thermal and electrical transport properties have been observed in the asymmetric shapes of nanoribbons⁵⁷⁻⁶⁰. All these observations may be related to the symmetric or asymmetric connection of the device to the leads and quantum interference⁶¹. The thermal and thermoelectric properties of the GNRs have been studied by Rojo *et al.*⁶², and Tan *et al.*¹⁰, for the vertical and parallel step-like junctions, respectively. However, there is still little information about the thermoelectric phenomena of hybrid junctions with different geometry and structural defects. This is especially true for the parallel step-like GSNRs, inspiring us to explore the thermal transport attributes in this type of hybrid nanostructures.

In this study, the spin caloritronic effects in the parallel step-like graphene/silicene nanoribbon (GSNR) junctions, including the divacancy, are numerically studied using the tight-binding (TB) and NEGF approaches. Three GSNRs with different length-to-width ratios are first selected and then subjected to the ferromagnetic exchange and local external electric fields. There are many experimental studies available in the literature, which have focused on developing various nanostructures^{40,63-69}, and measuring their spin thermoelectric properties^{70,71}. However, this paper numerically investigates the thermoelectric properties of parallel step-like GSNRs because: (1) the nanoribbons can satisfactorily show thermoelectric performance compared to their corresponding 2D structures⁷² (2) the step-like nanostructures can provide some unusual thermal and electrical transport properties for the asymmetric shape of nanoribbons⁶² (3) the hybrid type of nanostructures can often provide superior thermoelectric properties compared to the similar materials with the single nanostructures³², and (4) the defected nanostructures can provide different thermoelectric properties of the nanoribbons. They can also provide more realistic simulations for the actual experimental tests⁷³. Nonetheless, the calculation of the spin thermoelectric properties of the considered GSNRs using

experimental methods is beyond the scope of the present research. Although there may be a difference between the results obtained by this research with those given by the actual experimental tests, the results of this study can suitably pave the way for the development of standard experimental methods and thermoelectric property assessment of the GSNRs. It is concluded that a nearly full spin filtering effect with spin-dependent localized transmission peaks near the chemical potential $\mu = 0$ can be obtained. Moreover, larger spin-dependent Seebeck coefficient and spin polarization efficiency are identified compared to those given by ⁷⁴⁻⁷⁶. To further study the thermoelectric properties of the GSNRs, three defect arrangements with different orientations are also considered for the larger case study, and their responses are re-evaluated. The results of the present study are summarized in the subsequent sections.

2. Device structure and computational details

Three different parallel step-like GSNR junctions are introduced using semi-infinite metallic AGNRs with different widths of the left and right leads, and a ZSNR in the central region ^{43,77}. Each left and right lead is generated by duplicating two different unit cells along the transport direction. As shown in figure 1, each system contains $2N_{AG} = 46, 70, \text{ and } 94$ carbon atoms in each unit cell in the left and $N_{AG} - 1$ in the right region. $N_{AS} = 6, 10, \text{ and } 14$ number of armchair silicon-atom chains are also considered for the central regions. The changes in the central region width are dependent on the left contact size. These step-like GSNR junctions are named 23GE-6SE-11GE, 35GE-10SE-17GE, and 47GE-14SE-23GE, respectively. To further study the divacancy effects on the electronic and thermoelectric properties of the selected devices, three different defect orientations are considered in the central scattering region. In this study, the pentagon-octagon-pentagon (5-8-5) defect type ^{78,79} is selected for the defective system. The DVs are also assumed to be duplicated with the periodicity of $l = 4$ ⁸⁰. Despite a DV in the nanostructure, an equal number of A- and B-sublattice sites are assumed in all cases (see figure 1). This can provide net magnetic moment per unit cell i.e., $m = (N_A - N_B) \mu_B = 0$ ⁸¹.

To obtain the spin caloritronic characteristics of the selected nanostructures, their electron transmissions are first determined using the NEGF method ⁸² and Landauer-Bütticker transport formula ⁸³. Because there is a weak coupling among the electrons and phonons, the electron-phonon interactions are ignored in this study ⁸⁴⁻⁸⁶. Thus, electronic transports can appropriately be assumed ballistic. The spin-flip scattering is also neglected. Hence, the spin-up and spin-down electron transports can singly be investigated. This is valid because the spin diffusion length in SE is in the order of several micrometers ⁸⁷. As shown in figure 1, the system is divided into three various segments, including the

left and right electrodes, and the central region. The generalized Hamiltonian for the system consists of several submatrices as follows:

$$H_T = H_L + H_R + H_C + H_{CL} + H_{CR}, \quad (1)$$

where H_L , H_R , and H_C are the Hamiltonian matrices of the isolated left electrode, right electrode, and the central region, respectively. These submatrices can be determined by using Eqs. (2) and (3). In Eq. (4), H_{CL} and H_{CR} are also defined by the hopping between the central region and the left and right electrodes, respectively. The Hamiltonian matrices are all determined using the TB method⁸⁸⁻⁹⁰.

$$H_{R(L)} = -t_{R(L)} \sum_{\langle i,j \rangle, \alpha} c_{i\alpha}^\dagger c_{j\alpha} + eE_{YG} \sum_{i,\alpha} Y_{iG} c_{i\alpha}^\dagger c_{i\alpha} + \text{H. c.}, \quad (2)$$

$$H_C = -t_C \sum_{\langle i,j \rangle, \alpha} c_{i\alpha}^\dagger c_{j\alpha} + i \frac{\lambda_{so}}{3\sqrt{3}} \sum_{\langle\langle i,j \rangle\rangle, \alpha, \beta} v_{ij} c_{i\alpha}^\dagger (\sigma_z)_{\alpha\beta} c_{j\beta} + M_Z \sum_{i,\alpha} c_{i\alpha}^\dagger \sigma_z c_{i\alpha} + \quad (3)$$

$$+ e l E_Z \sum_{i,\alpha} \xi_i c_{i\alpha}^\dagger c_{i\alpha} + e E_{YS} \sum_{i,\alpha} Y_{iS} c_{i\alpha}^\dagger c_{i\alpha} + \text{H. c.},$$

$$H_{CR(CL)} = -t_{CR(CL)} \sum_{\langle i,j \rangle, \alpha} c_{i\alpha}^\dagger c_{j\alpha} + \text{H. c.}, \quad (4)$$

in which $t_{R(L)}$ and t_C are the hopping energies for the nearest-neighbor interactions in the right (left) lead, and the central region, respectively. In this study, 2.66 and 1.60 eV values are assumed for $t_{R(L)}$ and t_C , respectively^{88,90}. $c_{i\alpha}^\dagger$ ($c_{i\alpha}$) denotes the fermion creation (annihilation) operator at site i . α also is the spin index. $\langle i, j \rangle$ and $\langle\langle i, j \rangle\rangle$ show the nearest-neighbor and second-nearest-neighbor atoms, respectively. The rest of parameters used in Eqs. (2) – (4) are defined as follows: λ_{so} is the effective spin-orbit interaction and is assumed equal to 3.9 meV and zero for the SE and GE nanoribbons, respectively⁸⁹. σ is the Pauli matrix. v_{ij} is a parameter equal to -1 ($+1$) for the clockwise (counterclockwise) hopping index about the Z -axis. $\xi_i = +1, -1$ is the valley index for the sublattices A and B , respectively. E_Z is a perpendicular electric field that can yield a voltage difference equal to $2elE_Z$ in which e is the electron charge and l is the half distance of the two sublattices. M_Z is the exchange field induced by the proximity effect of ferromagnetic material⁹¹. E_{YG} and E_{YS} are the inhomogeneous transverse electric fields along y -direction, and applied to the leads and central region, respectively. Y_{iG} and Y_{iS} denote the y -coordinate of the atom i in the SE and GE nanoribbons. In this study, the electric and ferromagnetic exchange fields are assumed to be 0.082 V/Å and 0.162 eV, respectively, and perpendicularly applied to the central region of the hybrid GSNRs. The effects of inhomogeneous transverse electric fields $E_{YS} = 0.917$ V/Å and $E_{YG} = 0.680$ V/Å are also considered. t_{CR} (t_{CL}) denotes the hopping energy between the central region and right (left) lead, respectively. In this study, Harrison's scaling law^{92,93} is used

to compute the contact hopping energies for the GE and SE at the interface. At the interface, the bond length between carbon and silicon atoms is 1.89 Å, and its corresponding hopping energy is calculated as $t_{\text{CR(CL)}}=1.88$ eV. It is worth mentioning that this value needs to be in the same order of $t_{\text{R(L)}}$ and t_{C} ⁴. The spin-dependent transmission function, T_{α} , is used to determine the thermoelectric properties of the nanostructures, and can be obtained by Eq. (5) and using NEGF formalism⁹⁴:

$$T_{\alpha}(E) = \text{Tr}[\Gamma_{\text{L},\alpha}(E)G_{\text{C},\alpha}(E)\Gamma_{\text{R},\alpha}(E)G_{\text{C},\alpha}^{\dagger}(E)], \quad (5)$$

where $\Gamma_{\text{R(L),}\alpha} = i(\Sigma_{\text{R(L),}\alpha} - \Sigma_{\text{R(L),}\alpha}^{\dagger})$ is the interaction between the right (left) lead with the scattering region, in which $\Sigma_{\text{R(L),}\alpha}$ is the right (left) self-energy⁹⁴. $\Sigma_{\text{R(L),}\alpha}$ includes the effect of two semi-infinite AGNRs on the scattering region. $G_{\text{C},\alpha}(E)$ also denotes the retarded spin Green's function of the scattering region, and can be expressed as follows⁹⁴:

$$G_{\text{C},\alpha} = [(E + i0^{+})\text{I} - H_{\text{C}} - \Sigma_{\text{L},\alpha} - \Sigma_{\text{R},\alpha}]^{-1}, \quad (6)$$

The temperatures in the left and right leads are set to T_{L} and T_{R} , respectively. Hence, the temperature difference can be obtained by $\Delta T = T_{\text{L}} - T_{\text{R}}$. Based on the Landauer-Büttiker formula, the spin-dependent current can be obtained by⁹⁵:

$$I_{\alpha} = \frac{e}{h} \int_{-\infty}^{+\infty} T_{\alpha}(E)[f_{\text{L}}(E, T_{\text{L}}) - f_{\text{R}}(E, T_{\text{R}})] dE, \quad (7)$$

where e and h are the electron charge and the Plank constant, respectively. $f_{\text{R(L)}}$ and $T_{\text{R(L)}}$ represent the average Fermi-Dirac distribution and the temperature for the right (left) lead, respectively. T_{α} is also the spin-dependent transmission. The net spin current is defined as $I_{\text{s}} = I_{\text{up}} - I_{\text{dn}}$ and calculated by Eq. (7). Considering a linear response regime (i.e., $\Delta T \cong 0$), the spin-dependent Seebeck coefficient can then be computed for each spin channel as follows⁹⁶:

$$S_{\alpha} = -\frac{1}{eT} \left(\frac{L_{1,\alpha}}{L_{0,\alpha}} \right). \quad (8)$$

where $L_{n,\alpha}$ is the intermediate function and defined as⁹⁵

$$L_{n,\alpha}(\mu, T) = -\frac{1}{h} \int (E - \mu)^n \frac{\partial f(E, \mu, T)}{\partial E} T_{\alpha}(E) dE, \quad (9)$$

where μ is the chemical potential. The spin and charge Seebeck coefficients can then be computed by $S_{\text{s}} = S_{\text{up}} - S_{\text{dn}}$ and $S_{\text{c}} = (S_{\text{up}} + S_{\text{dn}}) / 2$, respectively⁹⁶. The electrical conductance is also defined as

$$G_{\alpha} = -e^2(L_{0,\alpha}). \quad (10)$$

where $G_c = G_{up} + G_{dn}$ and $G_s = |G_{up} - G_{dn}|$ is the charge and spin thermal conductance, respectively⁹⁷. The spin-dependent electron thermal conductance is obtained as⁹⁸

$$\kappa_{e,\alpha} = \frac{1}{T} \left(L_{2,\alpha} - \frac{L_{1,\alpha}^2}{L_{0,\alpha}} \right). \quad (11)$$

$$Z_{e,c(s)}T = S_{c(s)}^2 G_{c(s)}T / \kappa_e. \quad (12)$$

where Z_eT is the electrical FOM and is defined as the upper limit of $ZT = S^2GT / (\kappa_e + \kappa_{ph})$ value, in which κ_{ph} and κ_e are the phonon's and electron thermal conductance, respectively. The maximum value of ZT occurs when κ_{ph} is very smaller than κ_e ^{99,100}.

3.1. Analyses and results

To numerically investigate the performance of the step-like GSNRs, three different length-to-width ratios (β) of the central region, i.e., $\beta \cong 0.9, 1.0,$ and 1.1 , are selected for the considered devices (see figure 1). To produce a step-like nanoribbon, it is assumed that the right contact in all cases has a half-width from the left one. Each device is subjected to perpendicular electric (E_Z) and ferromagnetic exchange (M_Z) fields in the central region. It is noted that both local E_Z and M_Z fields¹⁰¹ can be produced in the laboratory environment. The effect of inhomogeneous transverse electric fields, i.e., E_{YS} and E_{YG} are also included for each system, respectively¹⁰². The electric current is also calculated by applying a difference between the temperature of the left, T_L , and the right, T_R , electrodes with no back gate voltage, and the spin currents are only determined in the presence of the temperature gradient.

In each system, a temperature gradient is generated between the two electrodes using $\Delta T > 0$. This can cause a nonzero value of $f_L - f_R$, and produce a spin-dependent current depending on $T_{R(L)}$ and ΔT . In addition, it creates changes in the spin-up and spin-down currents in the GSNRs at different step-like junctions. The thermal SFE is studied for the considered hybrid step-like GSNRs with threshold temperature (T_{th}). The variations of the spin-dependent current I_{up} (I_{dn}) versus T_R with $\Delta T = 10, 20,$ and 40 K are shown in figures 2a to 2c, representing small to large step-like GSNRs. As shown in these figures, when T_R increases, I_{up} reaches its maximum value for the high temperatures, whereas I_{dn} value is almost zero and remains unchanged for the whole temperature range. Moreover, the spin-up current is positive ($I_{up} > 0$) for almost $T_R > 100$ K, while the spin-down current $I_{dn} \cong 0$ throughout. The results show that the considered

GSNRs can well show an insulating response with no charge or spin current for nearly $T_R < 100$ K. For example, the threshold temperature value $T_{th} = 50$ K occurs at $\Delta T = 40$ K for the 23GE-6SE-11GE, whereas this value for the 35GE-10SE-17GE and the 47GE-14SE-23GE cases is similarly equal to 30 K. In addition, T_{th} marginally decreases by increasing the GSNR size. This is dependent on where the peak of spin-up transmission occurs as the system size changes (see figure 4). Thus, T_{th} value can be controlled by changing the system size. This clearly illustrates that the SFE¹⁵ is accompanied by the spin switching effect in these cases. As shown in figures 2b and 2c, the SFE is stronger when the device size increases. The peak values of I_{up} are almost obtained as 4.2, 10.24, and 10.83 nA for the 23GE-6SE-11GE, 35GE-10SE-17GE, and 47GE-14SE-23GE case studies, respectively (see figures 2a to 2f). Thus, the strength of the current varies when the device size is changed. However, the NDTR happens for the higher temperatures and ΔT . Accordingly, the hybrid step-like GSNRs can be utilized as a thermal spin device with multiple different characteristics. Figures 2d to 2f also show the changes of I_{up} and I_{dn} against ΔT for $T_R = 200, 250,$ and 350 K, respectively. These figures demonstrate that I_{up} increases as T_R and ΔT increase, while I_{dn} keeps nearly zero for various ΔT values. This again confirms that the thermal SFE has been generated. A thermal rectification behavior is also observed for the lower T_R and larger size of devices (see inset of figure 2f).

Figure 3 shows the variation of the spin polarization efficiency SPE ($= (|I_{up}| - |I_{dn}|) / (|I_{up}| + |I_{dn}|) \times 100\%$) versus T_R and ΔT for the studied systems. The results illustrate that the considered step-like GSNR junctions can suitably provide a thermal spin current with high SPE. The SPE of the devices is often dependent on the temperature sets and, most notably, on their sizes. Therefore, it is not appropriate to study the SPE below the ‘on-off’ temperature for the spin-up currents, where the spin-up and spin-down channels are closed. The results show that a nearly 100% SPE can be achieved for a broad range of T_R and ΔT values. This is especially true for the 47GE-14SE-23GE configuration (see figures 3e and 3f). Figure 3 also shows that SPE experiences sudden changes for a limited range of temperatures in some cases. This is due to the I_{up} reverse sign and the mutual competition among I_{up} and I_{dn} within this range of temperatures (See insets in figure 3). The SPE values larger than 99.80% and 99.99% can also be observed for the second and third case studies for the different values of ΔT at $T_R = 200$ K, respectively, whereas a nearly 93.0% value is obtained for the first case. This evidence confirms that the GNR and SNR-based devices often show less SPE values than their corresponding studied counterparts^{74,75,103}. The results of numerical analyses clearly show that the response of a hybrid nanostructure strongly depends on the values selected for the external electric and ferromagnetic exchange fields. The value of the fields in the present study has been chosen in such a way that we obtain the SFE and maximize

its efficiency. The results demonstrate that the selected magnitudes can provide high-efficiency value up to 99.9% in some case studies. It is noted that such a high SFE value has previously been obtained and reported by other researchers (e.g.,¹⁰⁴⁻¹⁰⁷).

The changes of the spin-polarized transmission coefficients (T_{up} and T_{dn}) against energy ($E - E_F$) and spin-dependent electrical conductance (G_{up} and G_{dn}) versus the chemical potential (μ) for the three studied cases are displayed in figure 4. In these plots, T_{up} (T_{dn}) and G_{up} (G_{dn}) are shown by a filled area and dotted line, respectively, and the Fermi level is set to zero. As shown in figure 4, the transmission peak values almost locally occur around the Fermi level i.e., the peak value of T_{up} almost occurs at [-0.16eV, -0.06eV], [-0.001eV, -0.07eV], and [-0.17eV, -0.07eV] intervals, for the 23GE-6SE-11GE, 35GE-10SE-17GE, and 47GE-14SE-23GE configurations, respectively. Nonetheless, they do not include a strong peak value for T_{dn} around the Fermi level. This is particularly true for the second and third configurations. This confirms that the spin-up governs the transport properties with $I_{up} > 0$, and can generate an almost perfect thermal SFE. The spin gap along with the narrow transmission peaks near the chemical potential $\mu = 0$ eV can lead to a larger spin-dependent Seebeck coefficient compared to the values provided by the GNRs and SNRs^{108,109}. Figure 4 clearly shows that G_{dn} is nearly zero in the spin-down channel for some ranges of μ values, whereas G_{up} is conductive in the spin-up channel. As a result, the proposed nanostructure device can provide a fully spin-polarized current.

Figure 5 shows the variation of S_{up} , S_{dn} , S_s , and S_c versus the chemical potential (μ) at $T_R = 300$ K. As shown in Figure 5, the response of S_{up} (S_{dn}) is not very identical around $\mu = 0$ eV for various sizes of nanoribbons. For each configuration, there are also some points at a given chemical potential value in which S_α (or thermal spin current) is equal to zero for one spin channel and is not zero for the other one; because the electron and hole currents are neutralized by one another. Hence, a perfect spin-polarized current can be obtained by the thermal gradient. Based on the results, the peak values of S_s around $\mu = 0$ eV are obtained as 0.404, 0.491, and 0.547 mV/K for the 23GE-6SE-11GE, 35GE-10SE-17GE, and 47GE-14SE-23GE case studies, respectively⁷⁶. The results also show that S_s can be increased as the device size is increased. This may be attributed to the fact that the spin gap gets larger. The peak value of $|S_s|$ occurs in the large chemical potential region and almost around $\mu = \pm 0.4$ eV, while the location of these peak values almost remained unchanged when the device size increases. The maximum values of $|S_s|$ for the 23GE-6SE-11GE, 35GE-10SE-17GE, and 47GE-14SE-23GE cases are obtained as 0.826, 1.150, and 1.114 mV/K, respectively. These values are very larger than the values reported in other researches (e.g., $S_s \sim 300$ μ V/K in^{97,98}, $S_s \sim 550$ μ V/K

in ⁷⁶, and $S_s \sim -90 \mu\text{V/K}$ in ¹⁰⁸). The color of S_s varies in accordance with the Seebeck polarization, $P_s (= (|S_{up}| - |S_{dn}|) / (|S_{up}| + |S_{dn}|))$ in figure 5. As shown in figure 5, S_s color varies from orange to black, representing the contribution of the spin-down and spin-up electrons in S_s , respectively. The charge and spin thermoelectric efficiencies are also assessed by calculating the electrical FOM ($Z_{e,c}T$ and $Z_{e,s}T$) for each case study and different μ values at room temperature (See insets of figure 5). The results show that the thermoelectric efficiency of a given device can significantly be improved as the size changes. The maximum values of the charge (spin) thermoelectric efficiencies occur about 15.06 (101.4), 13.4 (49.2), and 4.5 (9.2) from the large to small devices, respectively. It is realized that the third nanostructure case study (i.e., 47GE-14SE-23GE) can provide the largest charge and spin thermoelectric efficiency and enhance Z_eT . This enhancement is very larger than that reported in ¹¹⁰. The obtained results illustrate that the engineering defects in step-like GSNRs can provide a quite acceptable spin thermoelectric efficiency. It is noted that Z_eT is always larger than ZT . Hence, high value for Z_eT is nonsense in reality. Low Z_eT values are important because they allow us to exclude unpromising materials.

3.2. The effect of DV orientation on spin caloritronics

In order to achieve complete spin-dependent thermoelectric properties of the step-like GSNR junctions, a set of DVs with three different orientations in the 47GE-14SE-23GE (i.e., DV1, DV2, and DV3) is created and are analytically assessed ^{78,111} (see figure 1c). The variation of I_{up} and I_{dn} against T_R for DV1, DV2, and DV3 cases and $\Delta T = 40$ K are displayed in figure 6. I_{up} and I_{dn} values for no vacancy (NV) defect configuration are also plotted for the sake of comparison. As shown in the inset of figure 6a, the spin and charge transporting channels are almost closed for the NV and DV3 cases for the entire temperature ranges. In contrast, the other cases (i.e., DV1 and DV2) respond as an insulator for $T_R < 40$ K. In DV1 and DV2 cases, I_{dn} almost remained unchanged and equal to zero for the entire range of temperatures, while I_{up} is significantly increased as T_R exceeds 40 K. This confirms that the SFE is along with the spin switching effect in these cases, and occur only due to the temperature gradient with no back gate voltage. The NDTR phenomenon occurs for the latter two cases. For each case, I_{up} absolute value also increases by T_R , while their flowing directions are opposite at a given T_{th} . Figure 6b also presents the variation of I_{up} (I_{dn}) against ΔT for $T_R = 350$ K. As shown in figure 6b, I_{up} almost linearly increases for the DV1, whereas it is decreased for the DV2.

The variations of SPE against T_R and ΔT are also separately plotted for DV1 and DV2 case studies in figure 7. $\Delta T = 40$ K and $T_R = 350$ K are assumed for these plots, respectively. An SPE value larger than 99.6% can be obtained for DV2 case and a broad range of T_R and ΔT values. This shows a nearly 0.5% SPE value difference between DV1 and

DV2⁷⁸. In the DV2 case, the maximum SPE value occurs for high T_R and low ΔT values. This is fully compatible with the results reported in figure 6. It is worth mentioning that a sudden drop can be seen in figure 7 for a limited range of T_R values. However, this is negligible and is not essential in practical applications.

Figure 8 shows the variations of T_{up} (T_{dn}) against $E - E_F$ and G_{up} (G_{dn}) versus μ for DV1 and DV2 cases. The plot indicates that the variation of DV orientation can change the values of T_{up} (T_{dn}) and G_{up} (G_{dn}), while keeping the spin-up electron as the dominant carrier in both cases. Comparing DV1 and DV2 cases shows that T_{up} is remarkably enhanced when the divacancy orientation is changed to DV1. Although the peak values occur around $\mu = 0$ eV in both cases, there are two peaks for DV1 case at $[-0.17\text{eV}, -0.07\text{eV}]$, whereas two peak values for DV2 case are in both sides of this point, i.e., the first peak at $[-0.17\text{eV}, -0.11\text{eV}]$ and the second one at $[0.07\text{eV}, 0.11\text{eV}]$ interval. This indicates that the current sign for the DV2 case is negative and changes to positive with the increase of T_R and NDTR. In DV1, the maximum values of T_{up} and G_{up} are almost obtained 30% and 90% larger than the stronger value in the DV2 (see figure 8). As a result, I_{up} in the DV2 case is negative and weaker. Nevertheless, the values of T_{dn} and G_{dn} are nearly zero in both cases and confirm the SFE. Accordingly, the spin-dependent transmission coefficient, the direction, and intensity of the current can be engineered using the DV orientation.

Figure 9 depicts the variation of S_{up} , S_{dn} , S_s , and S_c versus μ for the studied cases at $T = 300$ K. By comparing S_s values obtained with the DV1 and DV2 configurations, we find that the change of DV orientation may vary S_s . As shown in figure 9, the maximum value of S_s is almost equal to 1.114 mV/K for the DV1 case, whereas, this value is 0.748 mV/K for the DV2 case. In the figure, S_s color varies from orange to black, representing the contribution of the spin-down and spin-up electrons in S_s , respectively. The charge and spin thermoelectric efficiency are also assessed by calculating the electrical FOM ($Z_{e,c}T$ and $Z_{e,s}T$) for each case study, and different μ values at room temperature (See insets in figure 9). The maximum values of $Z_{e,c}T$ and $Z_{e,s}T$ for the DV1 case are relatively 14% and 99% higher than those obtained by the DV2 case. This provides evidence that the thermoelectric efficiency of the case studies is controlled and enhanced by the DV.

4. Conclusions

In this research, the thermal SFE, spin-dependent electronic, and thermoelectric properties of the defected step-like GSNR junctions have numerically been studied. Each configuration was then subjected to the ferromagnetic exchange and local external electric fields. The divacancy effects were considered in the studied cases using the pentagon-

octagon pentagon (5-8-5) type model. Higher amounts of spin-up current were also determined for high-temperature values, while the spin-down current is remained unchanged and equal to zero for all temperature values, when the right lead temperature (T_R) increases. Hence, a satisfactory SFE and a spin polarization up to 99.99% were obtained in the studied GSNR junctions. The magnitude of the electric and ferromagnetic exchange fields is optimally selected to achieve the spin filtering effect with maximum efficiency. However, the SFE and current strength become more robust when the device size increases. This response behavior with localized transmission peaks could be achieved around the Fermi level if the divacancy was well oriented in the nanostructure. This provides evidence that the spin-dependent transmission coefficient, the direction, and intensity of the current can be engineered using the DV orientation. The NV and DV3 case studies showed insulator behavior, whereas the two other cases showed spin filtering behavior but with opposite spin current directions. It is realized that the DV1 case study (i.e., 47GE-14SE-23GE) can provide the strongest SFE and largest spin thermoelectric efficiency and enhance $Z_e T$. Some interesting transport properties such as the spin switching effect, rectifying behavior of the devices, and NDTR in thermal charge current were also observed. The maximum values of $|S_s|$ and the charge (spin) thermoelectric efficiencies for the 47GE-14SE-23GE case are obtained as 1.114 mV/K and 15.06 (101.4), respectively. These values are satisfactory and may be comparable to the values reported in other studies^{98,108,110}. In general, the considered hybrid GSNRs can be used for thermoelectric applications using different system temperature sets.

*Corresponding author: Farhad Khoeini (khoeini@znu.ac.ir)

References

- 1 Cowen, L. M., Atoyo, J., Carnie, M. J., Baran, D. & Schroeder, B. C. Organic materials for thermoelectric energy generation. *ECS Journal of Solid State Science and Technology* **6**, N3080 (2017).
- 2 Cui, C. *et al.* Bayesian optimization-based design of defect gamma-graphyne nanoribbons with high thermoelectric conversion efficiency. *Carbon* (2021).
- 3 Xiong, Y. *et al.* Chemically Switchable n-Type and p-Type Conduction in Bismuth Selenide Nanoribbons for Thermoelectric Energy Harvesting. *ACS nano* (2021).
- 4 Zhang, Z., Xie, Y., Peng, Q. & Chen, Y. A theoretical prediction of super high-performance thermoelectric materials based on MoS₂/WS₂ hybrid nanoribbons. *Scientific reports* **6**, 1-8 (2016).
- 5 Bauer, G. E., Saitoh, E. & Van Wees, B. J. Spin caloritronics. *Nature materials* **11**, 391-399 (2012).
- 6 Goennenwein, S. T. & Bauer, G. E. Electron spins blow hot and cold. *Nature nanotechnology* **7**, 145-147 (2012).
- 7 Kuschel, T. & Reiss, G. Charges ride the spin wave. *Nature nanotechnology* **10**, 22-24 (2015).
- 8 Uchida, K. *et al.* Observation of the spin Seebeck effect. *Nature* **455**, 778-781 (2008).
- 9 Fu, H.-H., Wu, D.-D., Zhang, Z.-Q. & Gu, L. Spin-dependent Seebeck effect, thermal colossal magnetoresistance and negative differential thermoelectric resistance in zigzag silicene nanoribbon heterojunction. *Scientific reports* **5**, 1-10 (2015).

- 10 Tan, X., Liu, L., Du, G.-F. & Fu, H.-H. Thermal transport and spin-dependent Seebeck effect in parallel step-like zigzag graphene nanoribbon junctions. *Physical Chemistry Chemical Physics* **22**, 19100-19107 (2020).
- 11 Zhai, X. *et al.* Spin-valley caloritronics in silicene near room temperature. *Physical Review B* **94**, 245405 (2016).
- 12 Zou, F., Zhu, L., Gao, G., Wu, M. & Yao, K. Temperature-controlled spin filter and spin valve based on Fe-doped monolayer MoS₂. *Physical Chemistry Chemical Physics* **18**, 6053-6058 (2016).
- 13 Khoeini, F., Shakouri, K. & Peeters, F. Peculiar half-metallic state in zigzag nanoribbons of MoS₂: Spin filtering. *Physical Review B* **94**, 125412 (2016).
- 14 Kim, W. Y. & Kim, K. S. Prediction of very large values of magnetoresistance in a graphene nanoribbon device. *Nature nanotechnology* **3**, 408 (2008).
- 15 Wu, D.-D., Du, G.-F. & Fu, H.-H. Spin-dependent Seebeck effect, and spin-filtering and diode effects in magnetic boron–nitrogen nanotube heterojunctions. *Journal of Materials Chemistry C* **8**, 4486-4492 (2020).
- 16 Li, L., Partoens, B., Xu, W. & Peeters, F. Electric-field modulation of linear dichroism and Faraday rotation in few-layer phosphorene. *2D Materials* **6**, 015032 (2018).
- 17 Mortazavi, B., Dianat, A., Cuniberti, G. & Rabczuk, T. Application of silicene, germanene and stanene for Na or Li ion storage: a theoretical investigation. *Electrochimica Acta* **213**, 865-870 (2016).
- 18 Neek-Amal, M., Sadeghi, A., Berdiyrov, G. & Peeters, F. Realization of free-standing silicene using bilayer graphene. *Applied Physics Letters* **103**, 261904 (2013).
- 19 Khoeini, F. & Jafarkhani, Z. Tunable spin transport and quantum phase transitions in silicene materials and superlattices. *Journal of Materials Science* **54**, 14483-14494 (2019).
- 20 Li, L., Partoens, B. & Peeters, F. Tuning the electronic properties of gated multilayer phosphorene: A self-consistent tight-binding study. *Physical Review B* **97**, 155424 (2018).
- 21 Anno, Y., Takei, K., Akita, S. & Arie, T. Enhancing the thermoelectric device performance of graphene using isotopes and isotopic heterojunctions. *Advanced Electronic Materials* **1**, 1500175 (2015).
- 22 Khalkhali, M., Rajabpour, A. & Khoeini, F. Thermal transport across grain boundaries in polycrystalline silicene: A multiscale modeling. *Scientific reports* **9**, 1-12 (2019).
- 23 Shirdel-Havar, M. & Farghadan, R. Armchair graphene nanoribbons with giant spin thermoelectric efficiency. *Physical Chemistry Chemical Physics* **20**, 16853-16860 (2018).
- 24 Zberekci, K., Swirkowicz, R., Wierzbicki, M. & Barnaś, J. Enhanced thermoelectric efficiency in ferromagnetic silicene nanoribbons terminated with hydrogen atoms. *Physical Chemistry Chemical Physics* **16**, 12900-12908 (2014).
- 25 Zong, P.-a. *et al.* Skutterudite with graphene-modified grain-boundary complexion enhances zT enabling high-efficiency thermoelectric device. *Energy & Environmental Science* **10**, 183-191 (2017).
- 26 Hicks, L. & Dresselhaus, M. S. Effect of quantum-well structures on the thermoelectric figure of merit. *Physical Review B* **47**, 12727 (1993).
- 27 Sierra, J. F. *et al.* Thermoelectric spin voltage in graphene. *Nature nanotechnology* **13**, 107-111 (2018).
- 28 Balandin, A. A. *et al.* Superior thermal conductivity of single-layer graphene. *Nano letters* **8**, 902-907 (2008).
- 29 Zberekci, K., Wierzbicki, M., Barnaś, J. & Swirkowicz, R. Thermoelectric effects in silicene nanoribbons. *Physical Review B* **88**, 115404 (2013).
- 30 Yang, X. *et al.* Temperature-controlled giant thermal magnetoresistance behaviors in doped zigzag-edged silicene nanoribbons. *RSC advances* **4**, 48539-48546 (2014).
- 31 Mahdaviifar, M., Shekarforoush, S. & Khoeini, F. Tunable electronic properties and electric-field-induced phase transition in phosphorene/graphene heterostructures. *Journal of Physics D: Applied Physics* **54**, 095108 (2020).
- 32 Wang, N., Han, L., He, H., Park, N.-H. & Koumoto, K. A novel high-performance photovoltaic–thermoelectric hybrid device. *Energy & Environmental Science* **4**, 3676-3679 (2011).
- 33 Parashchuk, T. *et al.* Insight into the transport properties and enhanced thermoelectric performance of n-type Pb_{1-x}Sb_xTe. *Journal of Alloys and Compounds* **860**, 158355 (2021).
- 34 Rostami, M., Ahmadi, I. & Khoeini, F. Highly tunable charge transport in defective graphene nanoribbons under external local forces and constraints: A hybrid computational study. *Results in Physics*, 103770 (2020).
- 35 Yousefi, F., Khoeini, F. & Rajabpour, A. Thermal conductivity and thermal rectification of nanoporous graphene: A molecular dynamics simulation. *International Journal of Heat and Mass Transfer* **146**, 118884 (2020).
- 36 Abdullah, N. R., Kareem, M. T., Rashid, H. O., Manolescu, A. & Gudmundsson, V. Spin-polarised DFT modeling of electronic, magnetic, thermal and optical properties of silicene doped with transition metals. *Physica E: Low-dimensional Systems and Nanostructures*, 114644 (2021).
- 37 Tromer, R. M. *et al.* Electronic, optical and thermoelectric properties of boron-doped nitrogenated holey graphene. *Physical Chemistry Chemical Physics* **22**, 21147-21157 (2020).
- 38 Gholami, Z. & Khoeini, F. Pure thermal spin current and perfect spin-filtering with negative differential thermoelectric resistance induced by proximity effect in graphene/silicene junctions. *Scientific Reports* **11**, 1-16 (2021).
- 39 Yang, K. *et al.* Enhanced thermoelectric properties in hybrid graphene/boron nitride nanoribbons. *Physical Review B* **86**, 045425 (2012).
- 40 Kiraly, B., Mannix, A. J., Hersam, M. C. & Guisinger, N. P. Graphene–silicon heterostructures at the two-dimensional limit. *Chemistry of Materials* **27**, 6085-6090 (2015).

41 Kistanov, A. A., Cai, Y., Zhang, Y.-W., Dmitriev, S. V. & Zhou, K. Strain and water effects on the electronic structure
and chemical activity of in-plane graphene/silicene heterostructure. *Journal of Physics: Condensed Matter* **29**, 095302
(2017).

42 Li, G. *et al.* Stable silicene in graphene/silicene Van der Waals heterostructures. *Advanced Materials* **30**, 1804650
(2018).

43 Liu, B. *et al.* Interface thermal conductance and rectification in hybrid graphene/silicene monolayer. *Carbon* **79**, 236-
244 (2014).

44 Drissi, L., Saidi, E., Bousmina, M. & Fassi-Fehri, O. DFT investigations of the hydrogenation effect on
silicene/graphene hybrids. *Journal of Physics: Condensed Matter* **24**, 485502 (2012).

45 Feng, Y. *et al.* Multiple synergistic effects of graphene-based hybrid and hexagonal born nitride in enhancing thermal
conductivity and flame retardancy of epoxy. *Chemical Engineering Journal* **379**, 122402 (2020).

46 Liu, B. *et al.* Interfacial thermal conductance of a silicene/graphene bilayer heterostructure and the effect of
hydrogenation. *ACS applied materials & interfaces* **6**, 18180-18188 (2014).

47 Ren, J. *et al.* Enhanced thermal conductivity of epoxy composites by introducing graphene@ boron nitride nanosheets
hybrid nanoparticles. *Materials & Design* **191**, 108663 (2020).

48 Chang, P.-H. & Nikolić, B. K. Edge currents and nanopore arrays in zigzag and chiral graphene nanoribbons as a route
toward high-Z T thermoelectrics. *Physical Review B* **86**, 041406 (2012).

49 Gunst, T., Markussen, T., Jauho, A.-P. & Brandbyge, M. Thermoelectric properties of finite graphene antidot lattices.
Physical Review B **84**, 155449 (2011).

50 Liu, Q.-B., Wu, D.-D. & Fu, H.-H. Edge-defect induced spin-dependent Seebeck effect and spin figure of merit in
graphene nanoribbons. *Physical Chemistry Chemical Physics* **19**, 27132-27139 (2017).

51 Oh, J. *et al.* Significantly reduced thermal conductivity and enhanced thermoelectric properties of single-and bi-layer
graphene nanomeshes with sub-10 nm neck-width. *Nano Energy* **35**, 26-35 (2017).

52 Yu, D., Lupton, E. M., Gao, H., Zhang, C. & Liu, F. A unified geometric rule for designing nanomagnetism in
graphene. *Nano Research* **1**, 497-501 (2008).

53 Chen, X., Liu, Y., Gu, B.-L., Duan, W. & Liu, F. Giant room-temperature spin caloritronics in spin-semiconducting
graphene nanoribbons. *Physical Review B* **90**, 121403 (2014).

54 Chico, L., Orellana, P., Rosales, L. & Pacheco, M. Spin and charge caloritronics in bilayer graphene flakes with
magnetic contacts. *Physical Review Applied* **8**, 054029 (2017).

55 Zhang, Z.-Y. & Guo, W. Cutting monolayer graphene into flexible spin filters. *Carbon* **115**, 43-49 (2017).

56 Sonvane, Y., Gupta, S. K., Raval, P., Lukačević, I. & Thakor, P. B. Length, width and roughness dependent thermal
conductivity of graphene nanoribbons. *Chemical Physics Letters* **634**, 16-19 (2015).

57 Ju, S. & Liang, X. Thermal rectification and phonon scattering in asymmetric silicon nanoribbons. *Journal of Applied
Physics* **112**, 024307 (2012).

58 Khoeini, F. & Shokri, A. A. Electronic transport in Bi-asymmetric T-shaped graphene nanoribbons. *Journal of
Computational and Theoretical Nanoscience* **8**, 740-745 (2011).

59 Yang, N., Zhang, G. & Li, B. Thermal rectification in asymmetric graphene ribbons. *Applied Physics Letters* **95**,
033107 (2009).

60 Zhang, Z., Wu, Z., Chang, K. & Peeters, F. Resonant tunneling through S-and U-shaped graphene nanoribbons.
Nanotechnology **20**, 415203 (2009).

61 Khoeini, F. & Shokri, A. Modeling of Transport in a Glider-Like Composite of GNR/CNT/GNR Junctions. *Journal of
Computational and Theoretical Nanoscience* **8**, 1315-1320 (2011).

62 Rojo, M. M. *et al.* Thermal transport across graphene step junctions. *2D Materials* **6**, 011005 (2018).

63 Chen, H. & Stoddart, J. F. From molecular to supramolecular electronics. *Nature Reviews Materials*, 1-25 (2021).

64 Chen, L. *et al.* Oriented graphene nanoribbons embedded in hexagonal boron nitride trenches. *Nature communications*
8, 1-6 (2017).

65 Fan, T. *et al.* Controllable size-selective method to prepare graphene quantum dots from graphene oxide. *Nanoscale
research letters* **10**, 1-8 (2015).

66 Kim, Y., Jeong, W., Kim, K., Lee, W. & Reddy, P. Electrostatic control of thermoelectricity in molecular junctions.
Nature nanotechnology **9**, 881 (2014).

67 Llinas, J. P. *et al.* Short-channel field-effect transistors with 9-atom and 13-atom wide graphene nanoribbons. *Nature
communications* **8**, 1-6 (2017).

68 Wang, H. S. *et al.* Towards chirality control of graphene nanoribbons embedded in hexagonal boron nitride. *Nature
Materials*, 1-6 (2020).

69 Wang, X. *et al.* Room-temperature all-semiconducting sub-10-nm graphene nanoribbon field-effect transistors.
Physical review letters **100**, 206803 (2008).

70 Reddy, P., Jang, S.-Y., Segalman, R. A. & Majumdar, A. Thermoelectricity in molecular junctions. *Science* **315**, 1568-
1571 (2007).

71 Widawsky, J. R. *et al.* Length-dependent thermopower of highly conducting Au–C bonded single molecule junctions.
Nano letters **13**, 2889-2894 (2013).

72 Unsal, E., Senger, R. & Sevinçli, H. Enhancement of thermoelectric efficiency of T– HfSe 2 via nanostructuring.
Physical Review B **103**, 014104 (2021).

73 Ni, Y. *et al.* Spin seebeck effect and thermal colossal magnetoresistance in graphene nanoribbon heterojunction. *Scientific reports* **3**, 1-5 (2013).

74 Huang, H., Zheng, A., Gao, G. & Yao, K. Thermal spin filtering effect and giant magnetoresistance of half-metallic graphene nanoribbon co-doped with non-metallic Nitrogen and Boron. *Journal of Magnetism and Magnetic Materials* **449**, 522-529 (2018).

75 Liu, Y. *et al.* Multi-functional spintronic devices based on boron-or aluminum-doped silicene nanoribbons. *Nanotechnology* **29**, 125201 (2018).

76 Zeng, M., Huang, W. & Liang, G. Spin-dependent thermoelectric effects in graphene-based spin valves. *Nanoscale* **5**, 200-208 (2013).

77 Matthes, L., Hannewald, K. & Bechstedt, F. Ab initio investigation of graphene-based one-dimensional superlattices and their interfaces. *Physical Review B* **86**, 205409 (2012).

78 An, R.-L. *et al.* Vacancy effects on electric and thermoelectric properties of zigzag silicene nanoribbons. *The Journal of Physical Chemistry C* **118**, 21339-21346 (2014).

79 Kim, Y., Ihm, J., Yoon, E. & Lee, G.-D. Dynamics and stability of divacancy defects in graphene. *Physical Review B* **84**, 075445 (2011).

80 Jippo, H., Ohfuchi, M. & Kaneta, C. Theoretical study on electron transport properties of graphene sheets with two- and one-dimensional periodic nanoholes. *Physical Review B* **84**, 075467 (2011).

81 Lieb, E. H. Two theorems on the Hubbard model. *Physical review letters* **62**, 1201 (1989).

82 Datta, S. *Quantum transport: atom to transistor*. (Cambridge university press, 2005).

83 Büttiker, M., Imry, Y., Landauer, R. & Pinhas, S. Generalized many-channel conductance formula with application to small rings. *Physical Review B* **31**, 6207 (1985).

84 Chen, A.-B., Wang, X.-F., Vasilopoulos, P., Zhai, M.-X. & Liu, Y.-S. Spin-dependent ballistic transport properties and electronic structures of pristine and edge-doped zigzag silicene nanoribbons: large magnetoresistance. *Physical Chemistry Chemical Physics* **16**, 5113-5118 (2014).

85 Gunlycke, D., Lawler, H. & White, C. Room-temperature ballistic transport in narrow graphene strips. *Physical Review B* **75**, 085418 (2007).

86 Kaneko, S., Tsuchiya, H., Kamakura, Y., Mori, N. & Ogawa, M. Theoretical performance estimation of silicene, germanene, and graphene nanoribbon field-effect transistors under ballistic transport. *Applied Physics Express* **7**, 035102 (2014).

87 Vogt, P. & Le Lay, G. *Silicene: Prediction, Synthesis, Application*. (Springer, 2018).

88 Liu, C.-C., Feng, W. & Yao, Y. Quantum spin Hall effect in silicene and two-dimensional germanium. *Physical review letters* **107**, 076802 (2011).

89 Mahdaviifar, M. & Khoeini, F. Highly tunable charge and spin transport in silicene junctions: phase transitions and half-metallic states. *Nanotechnology* **29**, 325203 (2018).

90 Reich, S., Maultzsch, J., Thomsen, C. & Ordejon, P. Tight-binding description of graphene. *Physical Review B* **66**, 035412 (2002).

91 Yokoyama, T. Controllable valley and spin transport in ferromagnetic silicene junctions. *Physical Review B* **87**, 241409 (2013).

92 Barrios-Vargas, J. E. *et al.* Electrical and thermal transport in coplanar polycrystalline graphene-hbn heterostructures. *Nano letters* **17**, 1660-1664 (2017).

93 Qasemnazhand, M., Khoeini, F. & Shekarforoush, S. Electronic transport properties in the stable phase of a cumulene/B7/cumulene molecular bridge investigated using density functional theory and a tight-binding method. *New Journal of Chemistry* **43**, 16515-16523 (2019).

94 Khoeini, F., Khoeini, F. & Shokri, A. Peculiar transport properties in Z-shaped graphene nanoribbons: A nanoscale NOR gate. *Thin solid films* **548**, 443-448 (2013).

95 Sivan, U. & Imry, Y. Multichannel Landauer formula for thermoelectric transport with application to thermopower near the mobility edge. *Physical review b* **33**, 551 (1986).

96 Wu, D. *et al.* Pure spin current generated in thermally driven molecular magnetic junctions: a promising mechanism for thermoelectric conversion. *Journal of Materials Chemistry A* **7**, 19037-19044 (2019).

97 Li, J., Wang, B., Xu, F., Wei, Y. & Wang, J. Spin-dependent Seebeck effects in graphene-based molecular junctions. *Physical Review B* **93**, 195426 (2016).

98 Wierzbicki, M., Swirkowicz, R. & Barnaś, J. Giant spin thermoelectric efficiency in ferromagnetic graphene nanoribbons with antidots. *Physical Review B* **88**, 235434 (2013).

99 Liu, J. *et al.* N-type organic thermoelectrics: demonstration of $ZT > 0.3$. *Nature communications* **11**, 1-9 (2020).

100 Mubarak, A. The mechanical, optical and thermoelectric properties of MCoF₃ (M= K and Rb) compounds. *Modern Physics Letters B* **31**, 1750033 (2017).

101 Le, P., Davoudiniya, M., Mirabbaszadeh, K., Hoi, B. & Yarmohammadi, M. Combined electric and magnetic field-induced anisotropic tunable electronic phase transition in AB-stacked bilayer phosphorene. *Physica E: Low-dimensional Systems and Nanostructures* **106**, 250-257 (2019).

102 Tran, V.-T., Saint-Martin, J. & Dollfus, P. Large on/off current ratio in hybrid graphene/BN nanoribbons by transverse electric field-induced control of bandgap. *Applied Physics Letters* **105**, 073114 (2014).

- 103 Liu, Y.-S., Wang, X.-F. & Chi, F. Non-magnetic doping induced a high spin-filter efficiency and large spin Seebeck
effect in zigzag graphene nanoribbons. *Journal of Materials Chemistry C* **1**, 8046-8051 (2013).
- 104 Pal, A. N. *et al.* Nonmagnetic single-molecule spin-filter based on quantum interference. *Nature communications* **10**, 1-
8 (2019).
- 105 Paudel, T. R. & Tsymbal, E. Y. Spin filtering in CrI₃ tunnel junctions. *ACS applied materials & interfaces* **11**, 15781-
15787 (2019).
- 106 Roch, J. G. *et al.* Spin-polarized electrons in monolayer MoS₂. *Nature nanotechnology* **14**, 432-436 (2019).
- 107 Tsai, W.-F. *et al.* Gated silicene as a tunable source of nearly 100% spin-polarized electrons. *Nature communications* **4**,
1-6 (2013).
- 108 Yang, X.-F., Liu, Y.-S., Feng, J.-F. & Wang, X.-F. Large spin Seebeck effects in zigzag-edge silicene nanoribbons. *AIP*
Advances **4**, 087116 (2014).
- 109 Zhai, M.-X. *et al.* Giant magnetoresistance and spin Seebeck coefficient in zigzag α -graphyne nanoribbons. *Nanoscale*
6, 11121-11129 (2014).
- 110 Sadeghi, H., Sangtarash, S. & Lambert, C. J. Enhancing the thermoelectric figure of merit in engineered graphene
nanoribbons. *Beilstein journal of nanotechnology* **6**, 1176-1182 (2015).
- 111 Palacios, J. J., Fernández-Rossier, J. & Brey, L. Vacancy-induced magnetism in graphene and graphene ribbons.
Physical Review B **77**, 195428 (2008).

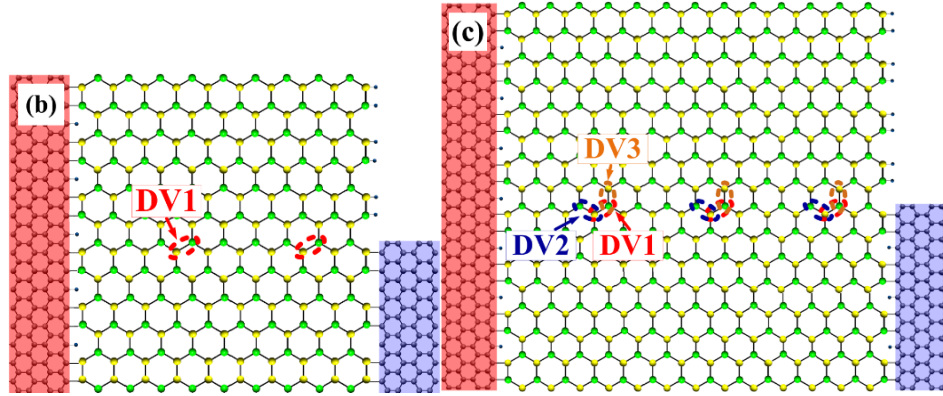
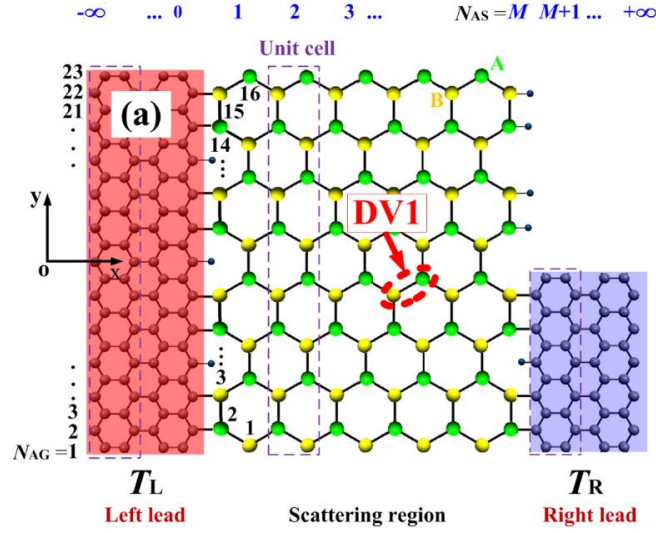


Figure 1. Schematic view of the defected parallel step-like GSNR junctions for (a) the 23GE-6SE-11GE, (b) the 35GE-10SE-17GE, and (c) the 47GE-14SE-23GE case studies. Each unit cell of the left lead has $2N_{AG}$ atoms. The central region is composed of about N_{AS} unit cells. Different DV orientations are also represented in the 47GE-14SE-23GE.

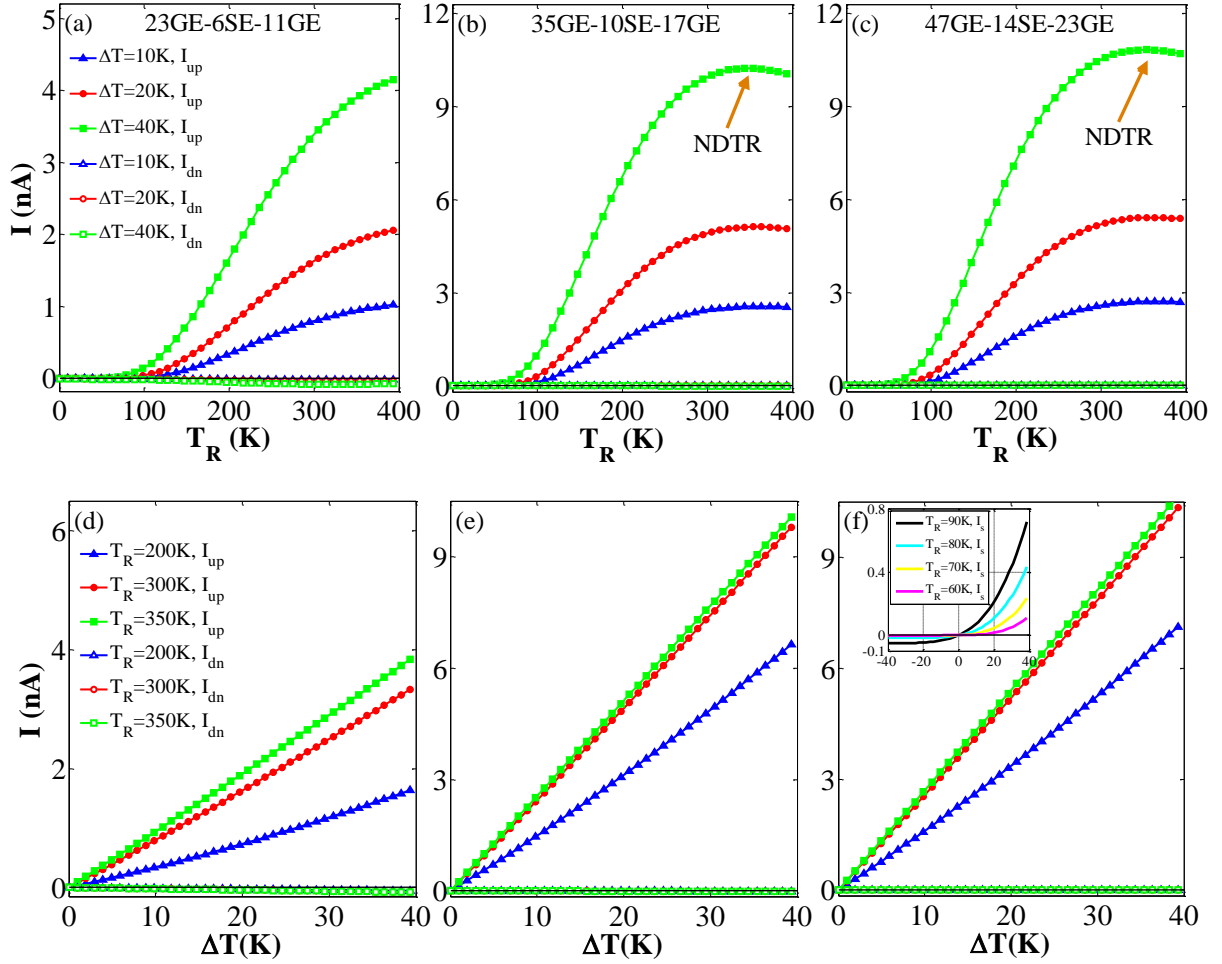


Figure 2. Panels (a), (b), and (c) show the variation of the spin-polarized currents (I_{up} and I_{dn}) against T_R for $\Delta T = 10, 20,$ and 40 K; Panels (d), (e), and (f) show I_{up} and I_{dn} against ΔT for $T_R = 200, 250,$ and 350 K for the 23GE-6SE-11GE, 35GE-10SE-17GE, and 47GE-14SE-23GE configurations, respectively.

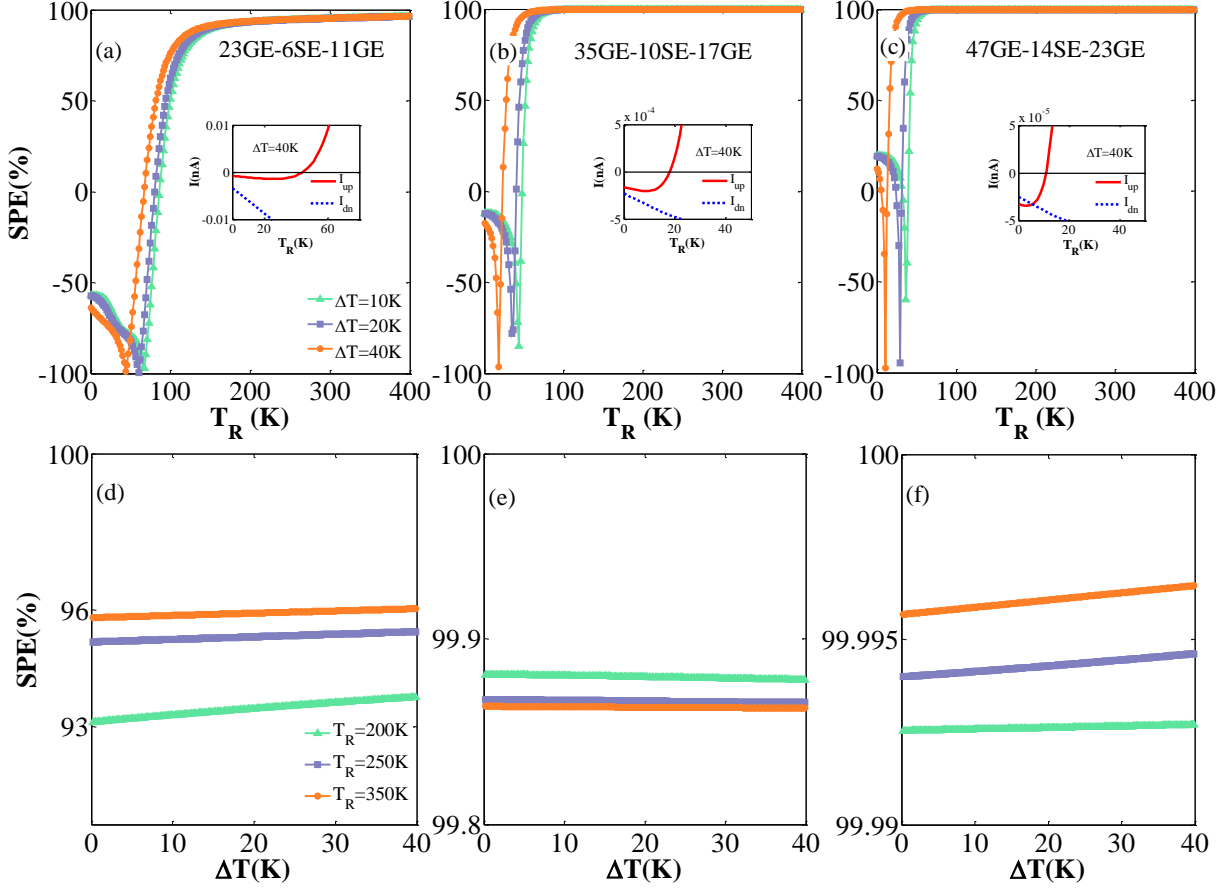


Figure 3. Panels (a), (b), and (c) show the variation of the SPE against T_R for $\Delta T = 10, 20,$ and 40 K; Panels (d), (e), and (f) show the SPE variation against ΔT for $T_R = 200, 250,$ and 350 K for the 23GE-6SE-11GE, 35GE-10SE-17GE, and 47GE-14SE-23GE configurations, respectively. The insets show the I_{up} reverse sign and the mutual competition among I_{up} and I_{dn} for $T_R < 100$ K and $\Delta T = 40$ K.

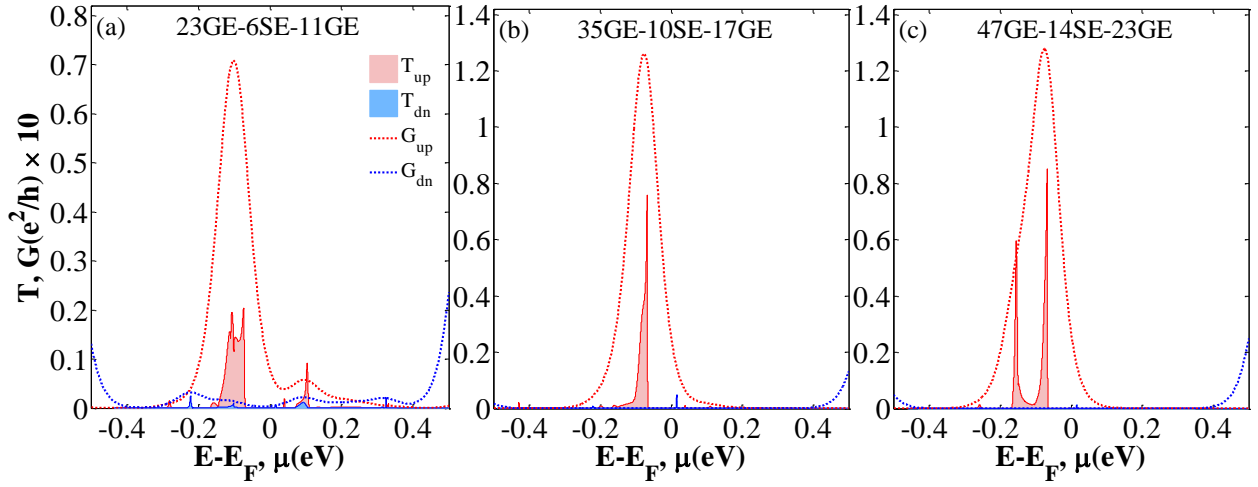


Figure 4. Panels (a), (b), and (c) show the variation of the spin-dependent transmission spectra (T_{up} and T_{dn}) against $E - E_F$ (filled area) and dotted lines show the variation of the spin-dependent electrical conductance (G_{up} and G_{dn}) versus μ for the 23GE-6SE-11GE, 35GE-10SE-17GE, and 47GE-14SE-23GE configurations, respectively, at $T = 300$ K.

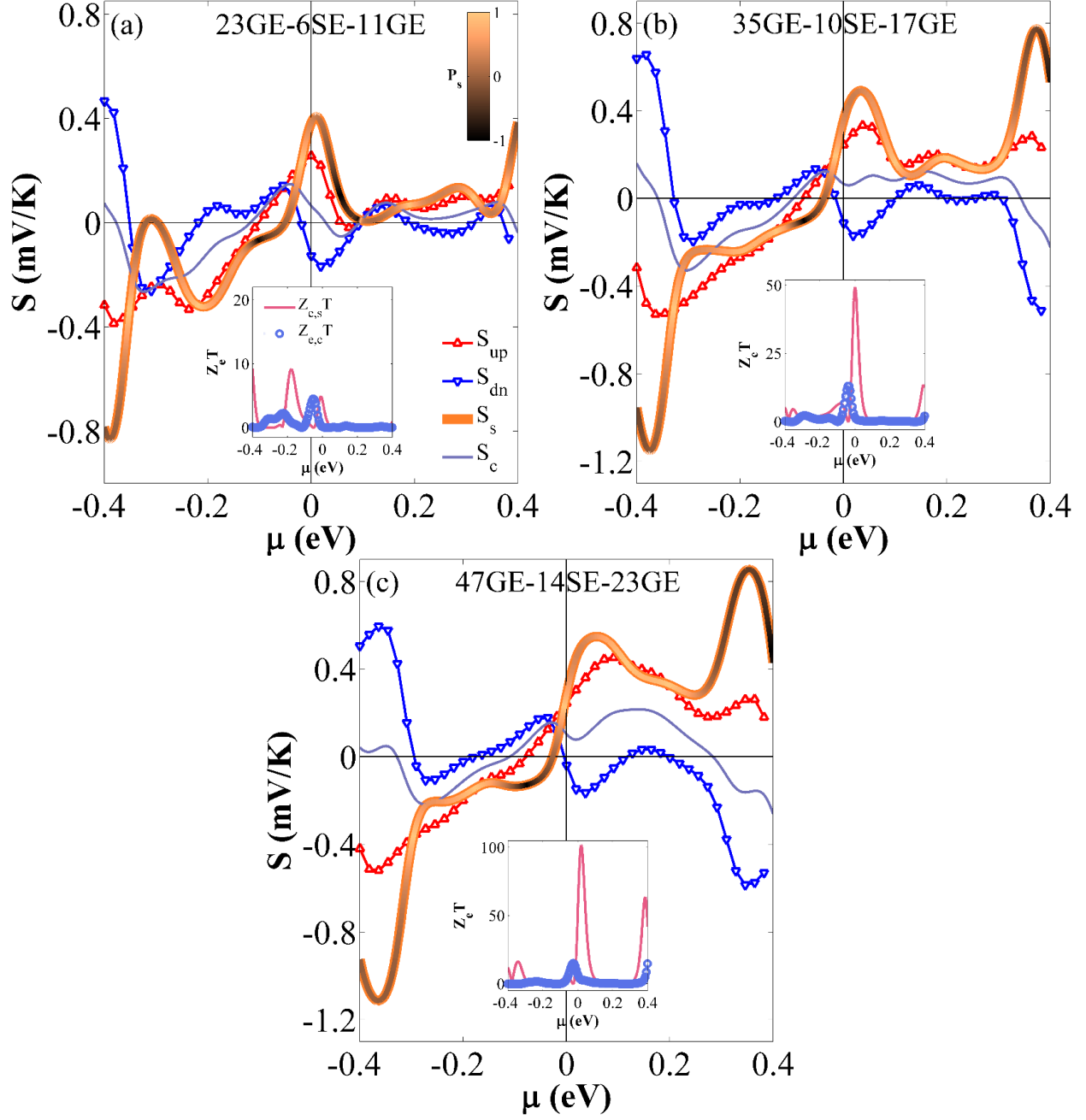


Figure 5. The S_{up} , S_{dn} , S_s , and S_c against μ at room temperature for (a), (b), and (c) 23GE-6SE-11GE, 35GE-10SE-17GE, and 47GE-14SE-23GE configurations, respectively. S_s color varies based on Seebeck polarization (P_s) value.

The insets show the $Z_{e,s}T$ and $Z_{e,c}T$ as a function of μ .

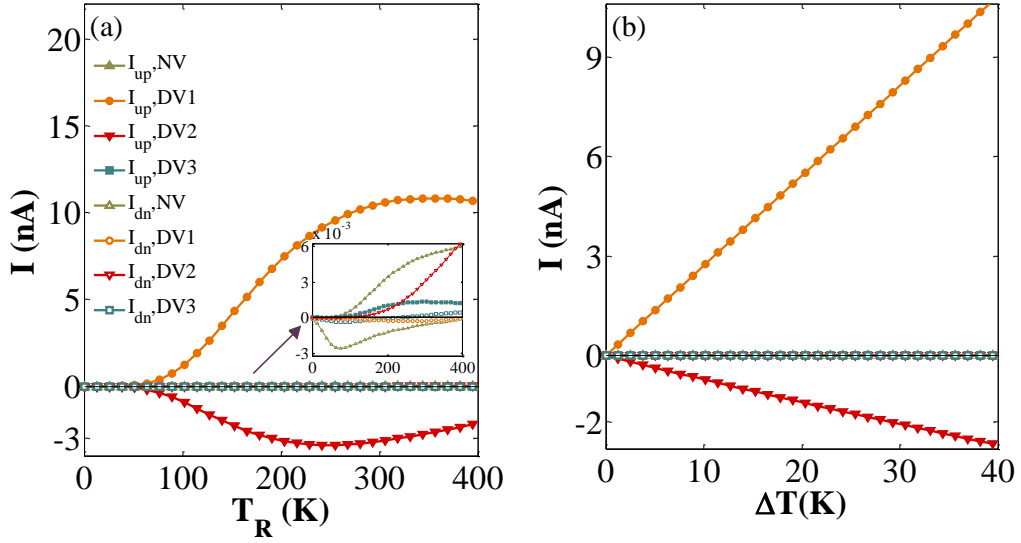


Figure 6. (a) I_{up} and I_{dn} versus T_R for $\Delta T = 40$ K; (b) I_{up} and I_{dn} versus ΔT for $T_R = 350$ K and NV, DV1, DV2, and DV3 configurations, respectively.

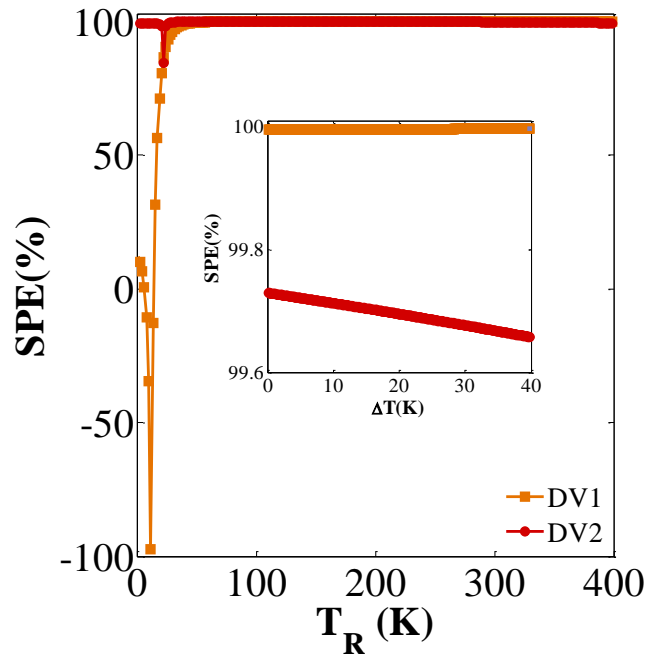


Figure 7. The SPE versus T_R for $\Delta T = 40$ K; The inset shows SPE versus ΔT for $T_R = 350$ K; for DV1 and DV2 configurations, respectively.

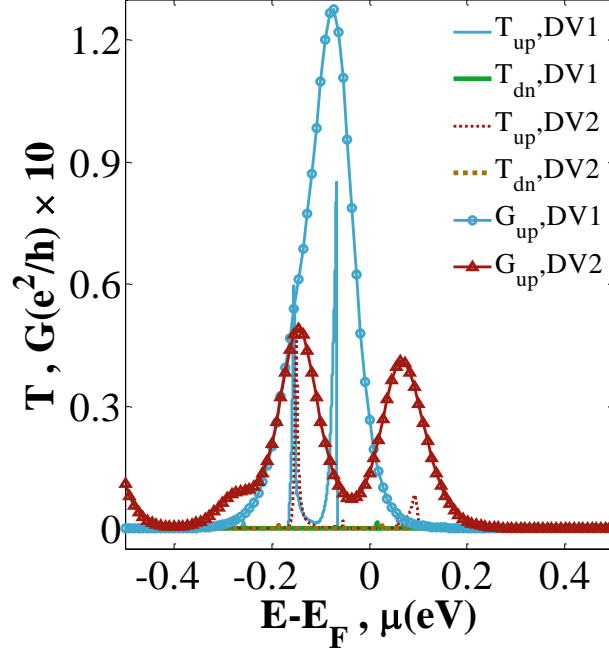


Figure 8. T_{up} and T_{dn} channels versus $E-E_F$, and G_{up} versus μ for the DV1 and DV2 configurations, at $T = 300$ K, respectively.

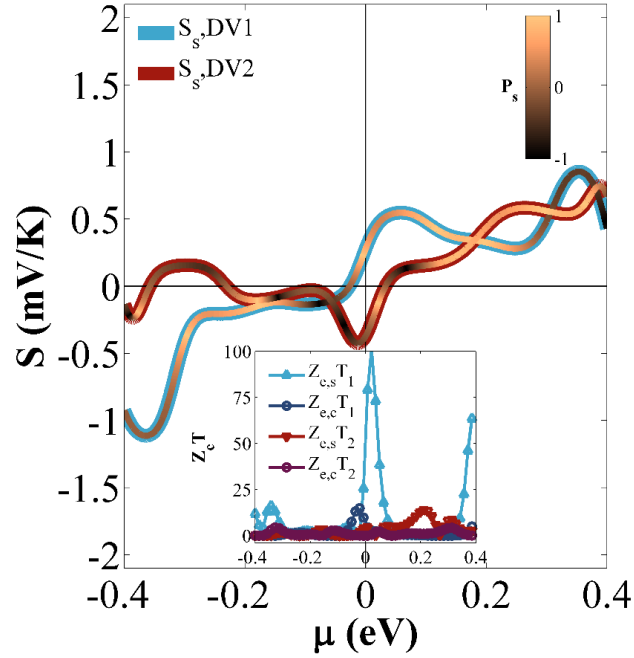


Figure 9. S_{up} , S_{dn} , S_s , and S_c against μ at room temperature for DV1 and DV2 cases, respectively. S_s color varies based on Seebeck polarization (P_s) value. The inset shows $Z_{e,s}T$ and $Z_{e,c}T$ as a function of μ .